Thermally Ultra-Robust $S = \frac{1}{2}$ Tetrazolinyl Radicals: Synthesis, Electronic Structure, Magnetism, and Nanoneedle Assemblies on Silicon Surface.

Zhimin Yang, $^{\dagger,\perp}$ Maren Pink, ‡ Ewa Malgorzata Nowik-Boltyk, § Shutian Lu, $^{\#}$ Tobias Junghoefer, § Suchada Rajca, † Stefan Stoll, $^{*,\#}$ Maria Benedetta Casu, *,§ and Andrzej Rajca *,†

†Department of Chemistry, University of Nebraska, Lincoln, Nebraska 68588-0304, USA. ‡IUMSC, Department of Chemistry, Indiana University, Bloomington, Indiana 47405-7102, USA. §Institute of Physical and Theoretical Chemistry, University of Tübingen, 72076 Tübingen, Germany. #Department of Chemistry, University of Washington, Seattle, Washington 98195, USA.

 $^{^{\}perp}$ Present address: Element Biosciences Inc., 10055 Barnes Canyon Rd, Suite 100, San Diego, CA 92121, USA.

Abstract:

Open-shell organic molecules, including $S = \frac{1}{2}$ radicals, may provide enhanced properties for several emerging technologies, however, relatively few synthesized to date possess robust thermal stability and processability. We report synthesis of $S = \frac{1}{2}$ biphenylene-fused tetrazolinyl radicals 1 and 2. Both radicals possess near-perfect planar structures based on their X-ray structures and DFT computations. Radical 1 possesses an outstanding thermal stability as indicated by the onset of decomposition at 269 °C, based on thermogravimetric analysis (TGA) data. Both radicals possess very low oxidation potentials < 0 V (vs. SCE) and their electrochemical energy gaps, $E_{cell} \approx 0.9$ eV, are rather low. Magnetic properties of polycrystalline 1 are characterized by SQUID magnetometry revealing a one-dimensional $S = \frac{1}{2}$ antiferromagnetic Heisenberg chain with exchange coupling constant $J'/k \approx -22.0$ K. Radical 1 in toluene glass possesses a long electron spin coherence time, $T_{\rm m} \approx 7~\mu {\rm s}$ in the 40 – 80 K temperature range, a property advantageous for potential applications as a molecular spin qubit. Radical 1 is evaporated under ultrahigh vacuum (UHV) forming assemblies of intact radicals on a silicon substrate, as confirmed by high-resolution X-ray photoelectron spectroscopy (XPS). Scanning electron microscope (SEM) images indicate that the radical molecules form nanoneedles on the substrate. The nanoneedles are stable for at least 64 hours under air as monitored by using X-ray photoelectron spectroscopy. EPR studies of the thicker assemblies, prepared by UHV evaporation, indicate radical decay according to first-order kinetics with a long half-life of 50 ± 4 days at ambient conditions.

INTRODUCTION

Recent advances in the design and synthesis of thermally robust high-spin di- and triradicals based on the Blatter radical, $^{1-6}$ have expedited the preparation of organic radical thin films via controlled evaporation under ultra-high vacuum (UHV). $^{1,4-6}$ Notable developments include thin films of a $S = \frac{1}{2}$ Blatter radical derivative exhibiting magnetic ordering 7 and a high-spin (S = 1) Blatter-based diradical with robust stability and electrical conductivity. 6 In addition, robustness and synthetic availability of $S = \frac{1}{2}$ Blatter radicals 8 enabled their recent applications as paramagnetic liquid crystals, 9,10 batteries, 11 and potential molecular spin qubits. 12 Likely, other novel properties will emerge from the remarkable Blatter radical, however, we are in search for new $S = \frac{1}{2}$ building blocks for future development.

2,2'-Biphenylene-fused tetrazolinyl (BFTZ) monoradicals, or so-called phototetrazolinyl radicals, ¹³ have attracted our attention because of their exceptional stability and, most importantly, the potential to achieve relatively large spin densities at the *para*-positions (and *ortho*-positions) with respect to the nitrogens of the tetrazolinyl moiety (Figure 1). Large spin densities at the *para/ortho* positions are the essential prerequisite in the design of high-spin polyradicals with large energy gaps between the high-spin ground state and low-spin excited state. ¹⁴⁻¹⁷

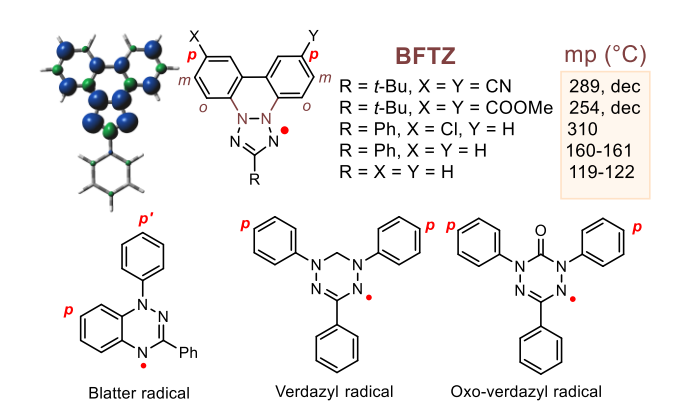


Figure 1. *Top*: 2,2'-Biphenylene-fused tetrazolinyl (BFTZ) radicals and spin density map at the UB3LYP/6-31G(d)+ZPVE level. *Bottom*: Blatter and verdazyl radicals. *Para*-positions are indicated with a red symbol p or p'.

Spin densities at the *para/ortho*-positions may be derived from experimental ${}^{1}H$ hyperfine couplings via the McConnell linear relationship, 18 that is, a larger hyperfine coupling corresponds to a greater spin density. For example, in the BFTZ radical (R = Ph, X = Y = H), the hyperfine coupling at the *para-*

position is $|A(^{1}H)| = 5.2 \text{ MHz.}^{19}$ In other nitrogen-centered stable radicals, analogous values of *para* $|A(^{1}H)|$ are 5.0 MHz (p) and 1.6 MHz (p') in the Blatter radical, 20,21 1.8 MHz in the oxo-verdazyl radical, 22 3.1 MHz in the verdazyl radical, 23 and only 2.7 MHz in simple tetrazolinyl radicals. 24

BFTZ radicals possess exceptional thermal stability. While the parent radical (R = X = Y = H) melts at about 120 °C,²⁵ its derivatives (R = t-Bu, X = Y = CN or CO_2Me) melt with decomposition at temperatures >250° C, according to the liturature.²⁴ Remarkably, a BFTZ derivative (R = Ph, X = Cl, Y = CN) was reported to melt at temperatures as high as ~300° C.^{20,21} Some of these radicals could be prepared not only in good yields, but also with nearly quantitative spin concentrations. Also, they were found to be monomeric in the solid state and in solution.^{13,19,24-26} In more recent studies, the mechanism of photochemical formation and ultrafast excited-state dynamics of tetrazolinyl radicals and 2,2'-biphenylene-fused tetrazolium cations (Figure 1: R = Ph, X = Y = H) were elucidated.^{27,28}

Here we report the synthesis and comprehensive characterization of $S = \frac{1}{2}$ 2,2'-biphenylene-fused tetrazolinyl radicals 1 and 2 (Figure 2). Radicals 1 and 2 are designed to take advantage of the exceptional stability of the BFTZ backbone, with the long-term goal of thermally and magnetically robust high-spin radicals. In particular, Br-substituted 2 would likely enable cross-coupling chemistry.

Figure 2. Radicals 1 and 2.

Both radicals were prepared as crystalline solids with near-perfect spin concentrations and characterized by X-ray crystallography, EPR spectroscopy (including electron spin relaxation properties for 1), SQUID magnetometry, voltammetry, UV-vis-NIR absorption spectroscopy and thermogravimetric analysis (TGA). Radical 1 was evaporated under UHV, forming, under the present preparation conditions, nanoneedles, as shown by scanning electron microscopy (SEM). The nanoneedles' UHV- and air-stability were further investigated by using X-ray photoelectron spectroscopy (XPS) and EPR spectroscopy.

The nanoneedle morphology is very interesting for nanoelectronics applications because of device miniaturization and the favorable ratio between surface and bulk that is beneficial for various devices such as sensors and transistors.²⁹⁻³² Several examples of small diamagnetic molecules, *p*- and *n*-type semiconductors, have been shown to grow following this morphology.³²⁻³⁷ However, to our knowledge, among adequately characterized thin films of radicals, only the tris(2,4,6-trichlorophenyl)methyl radical shows a mixed morphology, with the coexistent presence of islands and fibers when grown on graphene.³⁸ Conversely, radical 1 shows a distinct nanoneedle self-assembled morphology under the present preparation conditions.

RESULTS AND DISCUSSION

Synthesis. Formazans **4** are synthesized using a phase transfer catalysis approach,³⁹⁻⁴¹ in which suspensions of diazonium salts, prepared in situ from 4-cyano- or 4-bromo-aniline, are added to hydrazone **3** in a mixture of dichloromethane (DCM) and water in the presence of tetraalkylammonium salt (Scheme 1). Oxidation of formazans **4** with *N*-bromo-succinimide (NBS) provides the tetrazolium salts **5**.^{24,41} Photochemical ring closure of **5** gives fused tetrazolium (phototetrazolium) salts **6**.^{24,25} Finally, reduction of salts **6**, using SnCl₂ under basic conditions in water/benzene under inert atmosphere, ²⁶ yields radicals **1** and **2**. Spin concentrations for all prepared samples of radicals are summarized in the SI.

Scheme 1. Synthesis of radicals 1 and 2.

X-ray crystallography. The structures of radicals 1 and 2 are confirmed by X-ray crystallography (Figure 3). In both radicals, the tetrazolinyl-and-biphenyl-fused moieties are planar. As illustrated by the

small values of the dihedral angles, the phenyl substituent connected to C1 is approximately co-planar with the planes defined by the phenyl group (C14-C19) and the tetrazolinyl/biphenyl (C1-C13, C20, C21, N1-N6, Br1) tilted relative to each other by 10.18(9)° and 1.2(2)° in **1** and **2**, respectively.

Both 1 and 2 crystallize in the monoclinic space group P2₁/n. However, one molecule of benzene per formula unit is co-crystallized with 1. The crystals of 2 that are obtained from either pentane/toluene (0.17-mm long needle) or pentane/ethyl acetate (0.87-mm long needle) possess identical structures at 153 and 296 K, respectively; in both structures, the Br and CN groups are disordered over two positions.

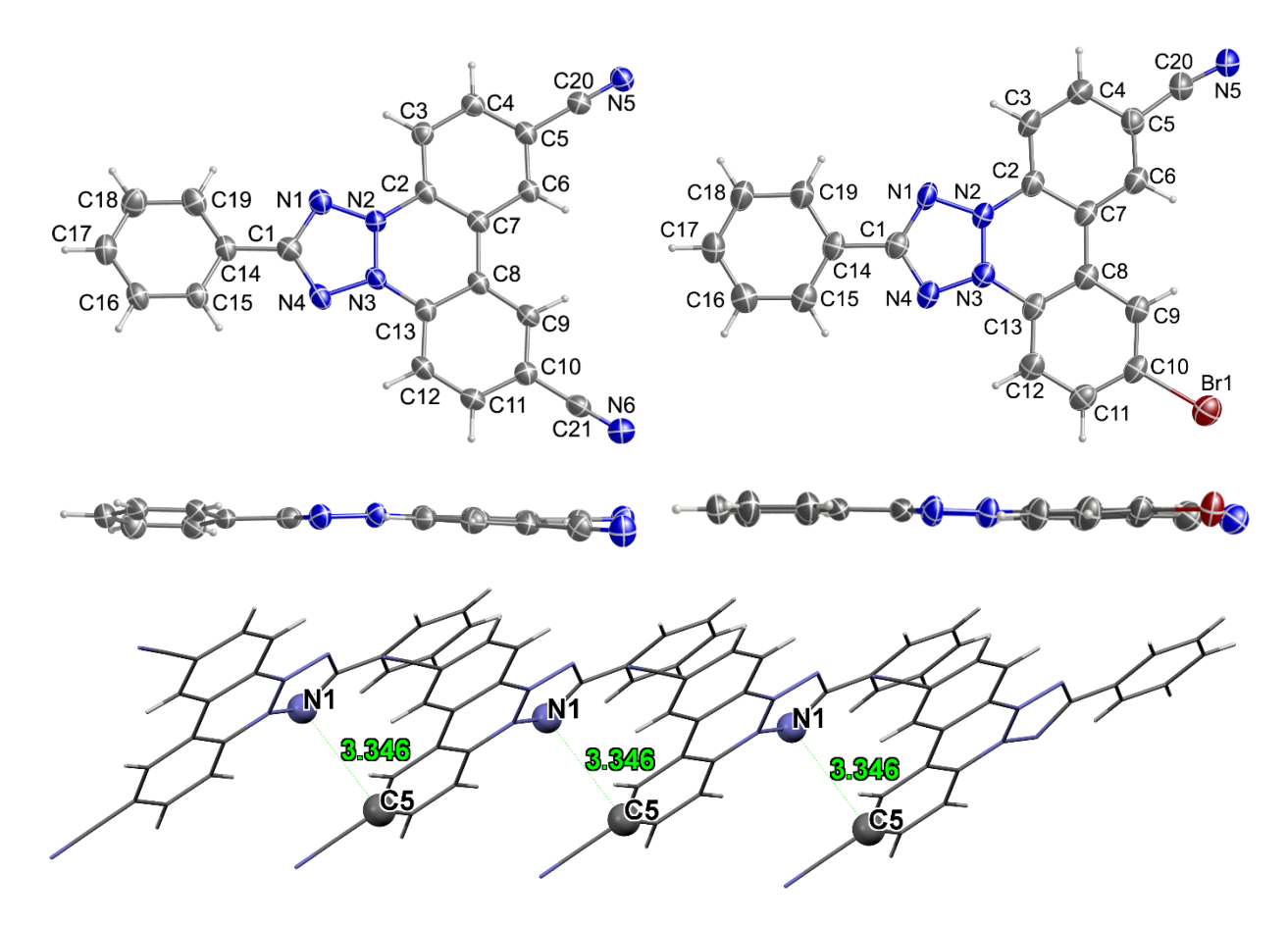


Figure 3. Molecular structure and crystal packing of **1** at 100 K and of **2** at 153 K. For **1**, a molecule of cocrystallized benzene is omitted. *Top* and *Middle*: Ortep plots (top and side views) with carbon, nitrogen, and bromine atoms depicted with thermal ellipsoids set at the 50% probability level (top and side views). For **1**, a molecule of co-crystallized benzene is omitted and for **2**, Br/CN disorder is not shown. *Bottom*: tetramer of molecules of **1** forming one-dimensional chain along the crystallographic *a*-axis with short intermolecular contacts, $N1\cdots C5 = 3.346$ Å. Further details are reported in Tables S1–S3 and Figures S1–S6, SI.

In the crystal of 1 at 100 K, the molecules are π -stacked, forming one-dimensional (1-D) chains along the crystallographic a-axis, with an average plane-to-plane distance of 3.28(9) Å, with planes defined by

the C/N atoms of the entire molecule (Figure 3). Because intermolecular close contacts, such as N1···C5 = 3.346 Å, 42 primarily involve atoms with positive spin densities, significant intermolecular antiferromagnetic interactions are anticipated in crystalline radical 1. Also, co-crystallized molecules of benzene magnetically isolate the 1-D chains (predominantly along the *c*-axis).

In the crystal of **2** at 153 K, the molecules are also π -stacked, forming alternating 1-D chains along the crystallographic a-axis, with plane-to-plane distances of 3.24(4) and 3.35(4) Å, when Br/CN disorder is not considered (planes defined by the Br/C/N atoms of the entire molecule). In the crystal of **2** at 296 K, 1-D chains with an average plane-to-plane distances of 3.40(4) Å are found, when Br/CN disorder is taken into account. For the nearest-neighbor molecules, intermolecular contacts, such as N1···C5 = 3.407 Å, are found. Thus, we anticipate that intermolecular antiferromagnetic interactions in **2** will be relatively weak and, most likely not 1-D, because of spatial proximity of 1-D chains in the crystal.

DFT computations. DFT (UB3LYP-D3BJ/6-31G(d,p)/PCM-UFF+ZPVE) optimized geometries for 1 and 2 in benzene (or DCM) indicate perfectly planar structures with C_{2v} and C_{s} symmetry, respectively.⁴³ In these computations, the UB3LYP functional is augmented with Grimme's empirical dispersion correction (D3 version)⁴⁴ and with the Becke–Johnson damping function.⁴⁵

Based on the relatively small value of the lowest vibrational frequency of 16 cm⁻¹ (*A*₂-symmetric mode) in **1**, primarily involving twisting of the phenyl group at C1 (Figure 3), we suspect that small distortions from planarity observed in the solid state structures of especially **1** are due to crystal packing effects. (For comparison in **2**, the lowest vibrational frequency of 22 cm⁻¹ is computed.) Both radicals follow the typical Aufbau rule, with electrons in their SOMOs at higher energy, compared to electrons in the corresponding HOMOs, in contrast to the SOMO/HOMO inversions found in selected nitrogencentered radicals.⁴⁶⁻⁵²

EPR spectroscopy. The purity of samples for radicals 1 and 2 is determined by EPR spectroscopic spin counting (SI). In addition, treatment of 1 with HCl in methanol/water at room temperature gives cleanly the 1-electron-oxidized product, i.e., diamagnetic tetrazolium cation 6-CN.

Neugebauer and Russell carried out 15 N labelling in symmetrically substituted BFTZ (X = Y) derivatives (Figure 1) 53 and established that the values of $A(^{14}$ N) ≈ 11 MHz associated with N1 and N4 (Table 1) were almost independent of substitution; the values of $A(^{14}$ N) $\approx 22-16$ MHz associated with N2 and N3 (Table 1) were following the relationship, CH₃ > H > CO₂CH₃ > CN. 19,24,53 Also, in the unsubstituted derivatives (X = Y = H), values of $A(^{14}$ H) at the *ortho* and *para* positions (Figure 1) were identical. 19

Due to significant spin densities at the four nitrogens of the tetrazolinyl moiety and at the *ortho*-carbons (and protons), CW EPR spectra of radicals **1** and **2** in benzene at room temperature show resolvable isotropic ¹⁴N and ¹H hyperfine couplings, $A(^{14}N)$ and $A(^{1}H)$ (Figure 4 and Table 1).⁵⁴

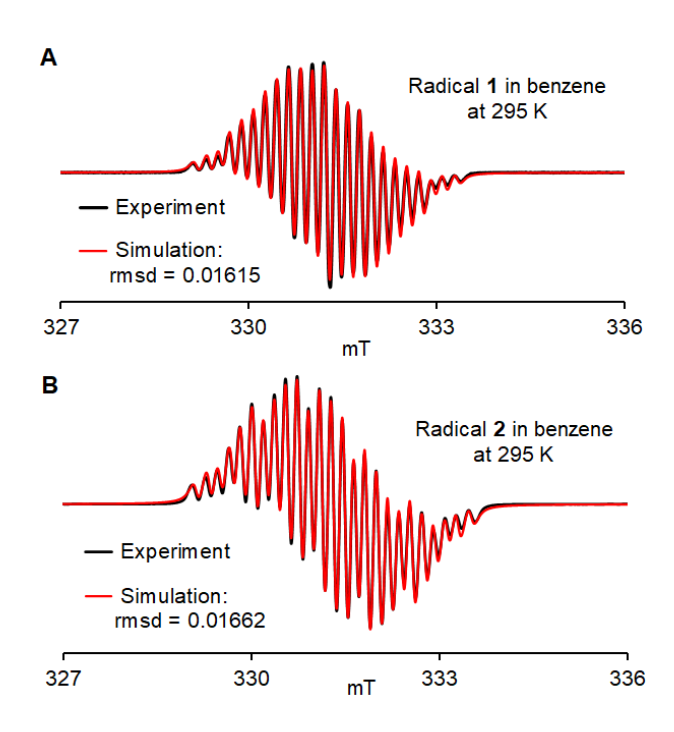


Figure 4. EPR spectra of radicals 0.29 mM **1** and ~0.2 mM **2** in benzene. **A**: 9.2918 GHz, modulation amplitude = 0.02 mT; simulation: 54 g = 2.0042, $A(^{14}N) = 15.79$ MHz (n = 2), $A(^{14}N) = 10.51$ MHz (n = 2), $A(^{1}H) = 5.74$ MHz (n = 2), linewidths peak-to-peak (lwpp), Gaussian = 0.00043 mT and Lorentzian = 0.1179 mT; **B**: 9.2956 GHz, modulation amplitude = 0.04 mT; simulation: 54 g = 2.0046, $A(^{14}N) = 20.10$ MHz (n = 1), $A(^{14}N) = 10.40$ MHz (n = 2), $A(^{14}N) = 14.79$ MHz (n = 1), $A(^{1}H) = 6.02$ MHz (n = 1), $A(^{1}H) = 5.64$ MHz (n = 1), lwpp, Gaussian = 0.00146 mT and Lorentzian = 0.1225 mT; g-values are uncorrected. Further details are in the SI: Table S4 and Figs. S19–S21.

Table 1. Summary of DFT-computed (UB3LYP-D3BJ/6-31G(d,p)/PCM-UFF+ZPVE in benzene) and experimental hyperfine coupling constants (*A* in MHz).

X P O H N2 N1 N3 N4 NC P O H							
	1 R = Ph			2 R = Ph			R = t-Bu
	X = CN			X = Br			X = CN
	DFT	EPR		DFT	EPR		EPR ^a
N_1	11.9	10.5		11.6	10.4		10.7
N_2	10.9	15.8		13.8	20.1		15.7
N_3	10.9	15.8		10.0	14.8		15.7
N ₄	11.9	10.5		11.9	10.4		10.7
H(0)	-7.2	5.8		-7.1 -7.9	5.6 6.0		5.0
N (CN)	1.6	-		1.8	-		-

a Ref 24.

The inclusion of unresolved ⁷⁹Br- and ⁸¹Br-hyperfine couplings at natural isotopic abundance, ⁵⁴ which serves as an effective additional line broadening contribution, provides an improved spectral fit for **2** (Fig. S21, SI). The resultant value of $A(^{79}Br) = 0.78$ MHz indicates a non-negligible amount of spin density on bromine, which is in qualitative agreement with the DFT computed $A(^{79}Br) = 1.7$ MHz (Table S4, SI).

We evaluate electron spin relaxation properties of 1 in frozen dilute toluene solution as a function of temperature. Longitudinal relaxation properties are measured using inversion recovery and fitted with an exponential recovery $V(T) = a - b \exp(-T/T_1)$, yielding the longitudinal relaxation time T_1 (Fig. S22, SI). As shown in Figure 5A, the relaxation rate, $1/T_1$, shows a steep monotonic increase with temperature, progressing from 0.033(5) ms⁻¹ at 19 K to 2.3(5) ms⁻¹ at 160 K.

To quantify the transverse relaxation, Hahn echo decays are measured and fitted with a stretched exponential decay $V(2\tau) = V(0) \exp(-(2\tau/T_{\rm m})^{\xi})$, yielding the electron spin phase memory (or coherence) time $T_{\rm m}$ and the stretch exponent ξ . The Hahn echo decays show substantial modulations due to ¹⁴N (see: Fig. S23, SI), which are neglected in the stretched-exponential model. As shown in Figure 5B, $1/T_{\rm m}$ shows a non-monotonic temperature dependence, in which it initially decreases to a minimum

of about $0.14(1) \,\mu\text{s}^{-1}$ around 60 K (corresponding to $T_{\rm m} \approx 7 \,\mu\text{s}$), before it increases until about 120 K. Values of $1/T_{\rm m}$ above 120 K are unreliable and associated with large uncertainties, since in this range the echo decay is on the same time scale as the period of the strong ¹⁴N nuclear echo modulation. We tentatively attribute the increased transverse relaxation rate at very low temperatures to the dynamics of the methyl groups of the solvent molecules (toluene- h_8). Protons on these methyl groups are responsible for enhancing decoherence. Such effects have been observed in a variety of other methyl-containing systems. ⁵⁵⁻⁵⁸ The decrease of the stretch exponent at low temperatures corroborates this interpretation.

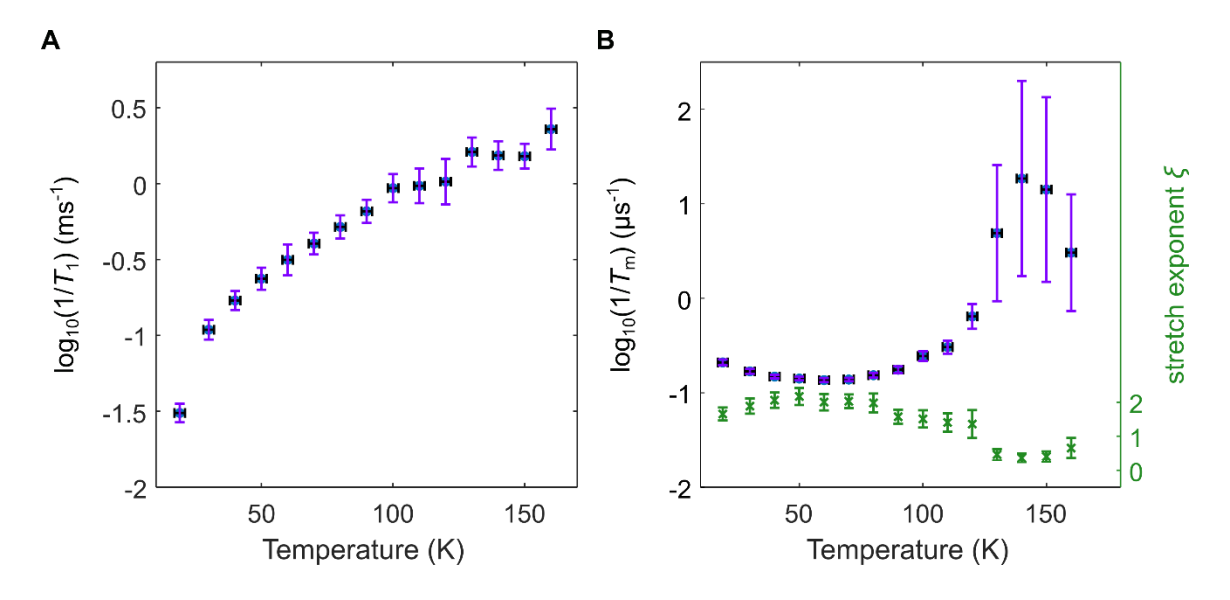


Figure 5. Relaxation properties of 1 at X-band (9.70 GHz, 346 mT). A. Temperature dependence of $1/T_1$ (blue circles) with experimental errors of temperature (black) and 95% confidence intervals of $1/T_1$ (purple). B. Temperature dependence of $1/T_m$ (blue circles, left axis) and the stretch exponent ξ (green crosses, right axis), including 95% confidence intervals. Values are listed in Table S5, SI.

One of the key prerequisites for the use of paramagnetic molecules as spin qubits for potential quantum sensing applications is a long coherence time $T_{\rm m}$.^{59,60} For 1 in toluene- h_8 , the value of $T_{\rm m}\approx 7~\mu {\rm s}$ in the 40 – 80 K temperature range is comparable to $T_{\rm m}=7.2~\mu {\rm s}$ for a Blatter radical derivative measured in toluene- d_8 at 25 K.⁶¹ The value of $T_{\rm m}\approx 7~\mu {\rm s}$ is significantly longer than $T_{\rm m}=3-4~{\rm and}~4-5~\mu {\rm s}$ in the 40 – 80 K range for typical gem-dimethyl and optimized spirocyclic pyrroline nitroxide radicals, respectively, ⁵⁸ or $T_{\rm m}=4-6~\mu {\rm s}$ and $T_{\rm m}<4~\mu {\rm s}$ in the 40 – 80 K range for Blatter radicals immobilized on silica and optimized vanadium complexes in protiated solvents/matrices, respectively.^{12,59,60}

SQUID magnetometry. Polycrystalline **1** and **2** are studied by SQUID magnetometry (Figs. S24–S27, SI). We focus on the study of radical **1** (Figure 6), because **1** exhibits much stronger exchange interactions, compared to **2**, as indicated by the values of mean-field parameters ($|\theta|$) differing by a factor of three (Fig. S26, SI). The value of $\chi T_{\text{max}} = 0.351$ emu K mol⁻¹ in the high temperature plateau (280 – 320 K) is in an excellent agreement with a spin concentration of 94%, as determined by EPR spin counting. At lower temperatures, the χT vs. T plot shows a profound downward turn, with crystal defects (magnetically isolated $S = \frac{1}{2}$ radicals), significantly contributing to the values of χT (and χ) at 1.8 K. The χ vs T plot has a characteristic broad maximum at $T_{\text{max}} \approx 14$ K, suggesting a low-dimensional magnetic behavior. Three sets of χ vs. T data may be well fit to one-dimensional (1-D) $S = \frac{1}{2}$ antiferromagnetic Heisenberg chain, $\frac{62-64}{2}$ to provide the coupling constant, $J'/k = -21.85 \pm 0.70$ K (mean \pm SE, n = 3). The common relationship for such 1-D chains, $T_{\text{max}}/|J'/k| = 0.641$, is well satisfied for radical **1**.62 Notably, another limiting model for such intermolecular antiferromagnetic coupling, such as pairs of S = 1/2 radicals (dimers), S = 1/2 radicals (dimers), S = 1/2 gives much inferior fits for the χ vs. S = 1/2 data (Fig. S25, SI). S = 1/2 radicals

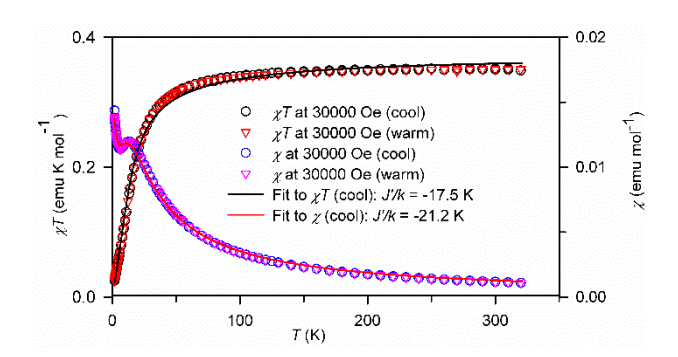


Figure 6. SQUID magnetometry of polycrystalline radical 1: experimental data plotted as χT vs. T and χT vs. T and the selected numerical fits to one-dimensional $S = \frac{1}{2}$ antiferromagnetic Heisenberg chain (Eqs. S1A and S1B, SI). Fitting parameters, such as J'/k and weight factors, and relevant statistical parameters are summarized in Table S6, and illustrated in Figs. S24–S27, SI.

Electrochemistry. Cyclic, differential pulse, and square wave voltammograms for radical 1 present approximately reversible processes with the oxidation and reduction peaks at $E^{+/0} \approx -0.14$ V and $E^{-/0} \approx -1.07$ V vs. SCE.⁶⁷ Because radical 2 is derived from 1 by replacing one of the strongly electron

withdrawing cyano groups with bromine, it is easier to oxidize at $E^{+/0} \approx -0.28$ V to the diamagnetic cation and slightly more difficult to reduce at $E^{-/0} \approx -1.14$ V (Figure 7).

The highly negative oxidation potentials (e.g., $E^{+/0} \approx -0.3$ V for 2) may impede its Pd-catalyzed cross-coupling reactions, as already observed for Blatter radicals with $E^{+/0} \approx +0.1$ –(+0.3) V,^{68,69} requiring a highly reactive Pd-catalyst,⁵ compared to oxo-verdazyl radicals with $E^{+/0} \approx +0.8$ V.^{70,71}

For radicals 1 and 2, electrochemical band gaps, $E_{\text{cell}} = E^{+/0} - E^{-/0}$, are rather low with $E_{\text{cell}} = 0.935 \pm 0.015$ and 0.866 ± 0.003 eV, respectively. Because E_{cell} may be related to the gas phase IP – EA and to disproportionation energies for the 2R \rightarrow R⁺ + R⁻ reaction, the low values of E_{cell} are one of the favorable factors in the design of neutral radical conductors. 6,72-75

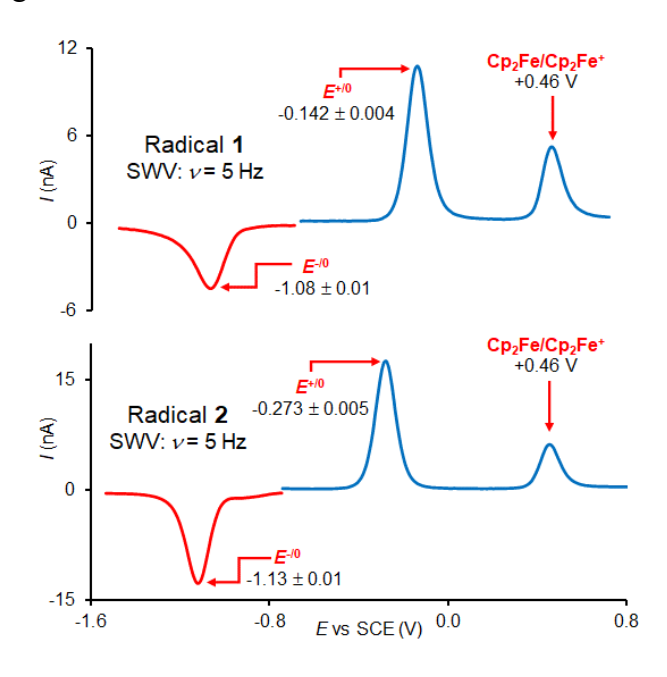


Figure 7. Square wave voltammetry (SWV) of radicals **1** and **2** in 0.1 M tetrabutylammonium hexafluorophosphate in dichloromethane at room temperature. Redox potentials are given as mean \pm stddev with n = 4-9 (**1**) and 6-9 (**2**). For further details, including cyclic and differential pulse voltammetries, see: the SI, Figs. S15–S18.

UV-vis-NIR spectroscopy. UV-vis-NIR spectra of 1 and 2 in dichloromethane (DCM) show the longest wavelength bands at $\lambda_{\text{max}} = 717-729$ nm with broad absorption envelopes (Figure 8). The spectrum for 1 can be reasonably well reproduced by TD-DFT computations (after shifting the computed band positions by -0.6 eV, Fig. S7, SI).⁴³ Plots of molar absorbance (extinction coefficient), ε , vs. wavenumber, \tilde{v} , for radical 1 in DCM and in benzene demonstrate that the longest wavelength band at

 $\lambda_{\rm max} \approx 730$ nm (the lowest wavenumber band at $\tilde{v}_{\rm max} \approx 13700$ cm⁻¹) is symmetrical, and it shows negligible solvent dependence (Figure 8, inset).

For radical 1 in DCM or benzene, the optical band gap, $E_g = 1.12 \pm 0.002$ eV, is slightly higher, compared to $E_g = 1.09$ eV for radical 2 in DCM (Figs. S9–S12, SI), which parallels the trend in the values of E_{cell} ; though for 1 in DCM, the longest wavelength band, $\lambda_{max} = 726-729$ nm, possesses a bathochromic shift, compared to corresponding $\lambda_{max} = 717$ nm for 2 in DCM. For comparison, BFTZ (R = t-Bu, X = Y = CN) radical in dioxane was reported to possess $\lambda_{max} = 695$ nm.²⁴ Diamagnetic cations (salts) 6-CN and 6-Br, precursors to 1 and 2, possess much higher $E_g = 2.50$ and 2.00 eV, respectively (Figs. S13 and S14).

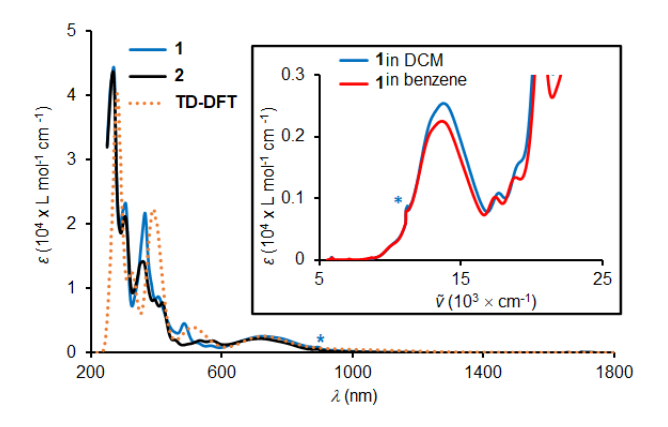


Figure 8. *Main plot:* UV–vis–NIR (294 K) absorption spectra for 0.31 and 0.30 mM radicals **1** and **2** in DCM, as well as TD-DFT computed spectrum for **1** in DCM solvent model. For **1**, bands at $\lambda_{\text{max}} = 270$, 306, 365, 406, 485, and 729 nm have the following extinction coefficients (L mol⁻¹ cm⁻¹): $\varepsilon_{270} = 4.4 \times 10^4$, $\varepsilon_{306} = 2.3 \times 10^4$, $\varepsilon_{365} = 2.2 \times 10^4$, $\varepsilon_{406} = 8.7 \times 10^3$, $\varepsilon_{485} = 4.5 \times 10^3$, and $\varepsilon_{729} = 2.5 \times 10^3$. The values of ε are not corrected for spin concentration of the radicals. *Inset plot:* Expanded spectra for **1** in DCM and benzene, plotted vs wavenumbers (\tilde{v}) and showing the longest wavelength band at $\lambda_{\text{max}} \approx 730$ nm. The feature at $\lambda \approx 900$ nm, marked with a blue asterisk, is an instrumental artifact (change of grating). Further details may be found in the SI: Figs. S7–S14.

Stability of radicals by TGA. Thermogravimetric analysis (TGA) data indicate that the onset of thermal decomposition of **1**, corresponding to a 1% mass loss, is at 269 °C. At 301 °C, the decomposition rate reaches a sharp maximum (with a shoulder at ~290 °C). In contrast, for **2**, the primary decomposition has the onset and maximum rate temperatures that are by 50–80 °C lower, and the secondary decomposition possesses a maximum rate at 338 °C (Figure 9).

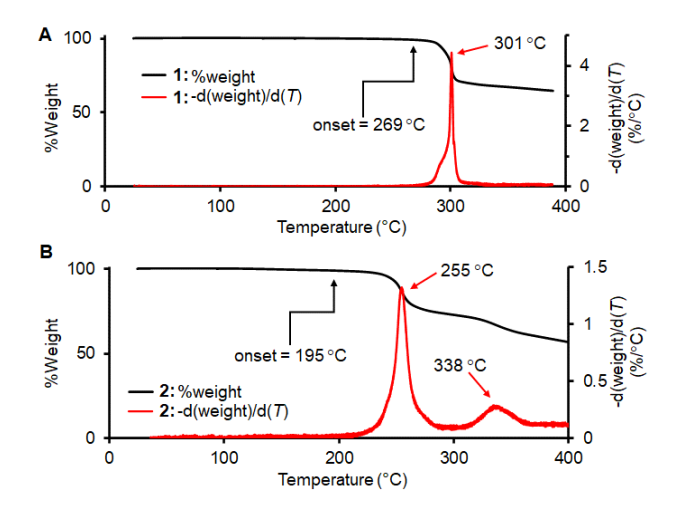


Figure 9. Thermogravimetric analysis (TGA) of radicals **1** (A) and **2** (B) under N_2 ; heating rate = 5 °C min⁻¹. Further details may be found in the SI: Figs. S28–S31.

We note that radical 1 in benzene at room temperature is quite persistent with about 3% (vs. TEMPONE) and 5% decrease of double integrated intensity of its EPR spectrum in one and two weeks, respectively; this corresponds to a half-life of the order of 5–6 months. As mentioned before, radical 1 in the presence of strong acid, such as concentrated HCl in methanol/water, at room temperature undergoes a nearly quantitative conversion to the precursor tetrazolium salt 6-CN (see: SI, Section 1.e).

Controlled deposition of radical 1 on SiO₂/Si(111) wafers. Using a well-established method, ^{76,77} we evaporated radical 1 on native SiO₂ on Si(111) wafers. We used organic molecular beam deposition (OMBD) which allows precise control of the evaporation parameters. ⁷⁸ The radical assemblies were investigated, without breaking the vacuum, by using XPS. This experimental technique, based on the photoelectric effect, can be used to determine quantitatively the concentration of the elements adsorbed onto a surface. ^{79,80} The intensity and binding energies of the spectroscopic lines are sensitive to the chemical environment of the elements forming the radicals. ⁷⁹ Thus, we were able to: 1) compare the core level spectra of the assemblies with those of the powder (i.e., with the signal from radical 1 that did not undergo evaporation, Figure 10); 2) calculate the stoichiometry of the obtained assemblies, comparing them to the molecular stoichiometry (Table S7, SI); and 3) fit the main spectroscopic line adopting a fit procedure that we developed for radicals ⁸¹ that allows assessing the integrity of the molecules and, therefore, their radical character (Figure 10).

Looking in detail at the C 1s and N 1s core-level spectra, we found that the main lines have a complex shape that mirrors the different chemical environments of each atom in the radical. The carbon atoms have two main different chemical environments: the emitted photoelectrons have different binding energies depending on whether they are bound to other carbon atoms and hydrogen atoms or to a nitrogen atom (see; the molecular structure in Figure 2, the fit analysis in Figure 10, and the corresponding Tables S8 and S9, SI). This is signaled by the C 1s spectroscopic line showing two contributions, the one at higher binding energy being the component due to photoemission of electrons from carbon atoms bound to nitrogen atoms. In a very simplified model, this can be understood in terms of electronegativity. Nitrogen atoms are more electronegative than carbon atoms. This moves the electronic cloud towards them, requiring more energy to emit an electron. A similar argument also holds for the N 1s spectroscopic line that, with its complex shape, mirrors the presence of the tetrazole ring, with four different chemical environments of the nitrogen atoms and the presence of the cyano-groups (see the molecular structure in Figure 2, the fit analysis in Figure 10, and Tables S10 and S11, SI). The fit assignment is also in very good agreement with previously investigated radical and closed-shell thin films. 1,61,82 In addition to the effects due to the different chemical environment, we also observe the presence of several satellite features, the so-called shake-up satellites, typical features in photoemission that appear as an effect of the relaxation processes, caused by the core-hole left behind by the photoemitted electron. Taking into account their intensity is mandatory to gain reliable information on the stoichiometry of the investigated systems. 79,80,83

The comparison of the spectra of the assembly with the spectra of the powder does not show new or different features (see: Figure 10).

In the tetrazolinyl ring, the chemical environments of the four nitrogen atoms are very similar, thus, within the experimental resolution, we expect a single asymmetric line, as it is the actual case both for powders and assemblies. This is consistent with previously published results on the diamagnetic tetrazole-based systems. 84-88 The main line at around 400 eV shows a pronounced shoulder. This suggests a stronger

delocalization/screening of the core hole created upon photoemission in one of the nitrogen atoms. Considering the crystal structure of radical 1 (Figure 3), we can infer that the intermolecular contact N1···C5 is short enough^{42,89-91} to enhance the screening of the core hole in N1, pushing the binding energy of the N1 photoemitted electrons toward the lower energy range. This behavior is the same for the assemblies and the powder (polycrystalline 1). This observation suggests that the nanoneedles are characterized by an arrangement of the molecules similar to the one of polycrystalline 1.

The result of this approach indicates that evaporation and deposition do not change the chemical structure of the molecules in the assemblies, i.e., the radical character and the molecules are wholly intact in the assembly, i.e., the deposition of radical 1 occurred without degradation. The assemblies were also investigated by using EPR spectroscopy that confirmed their radical character.

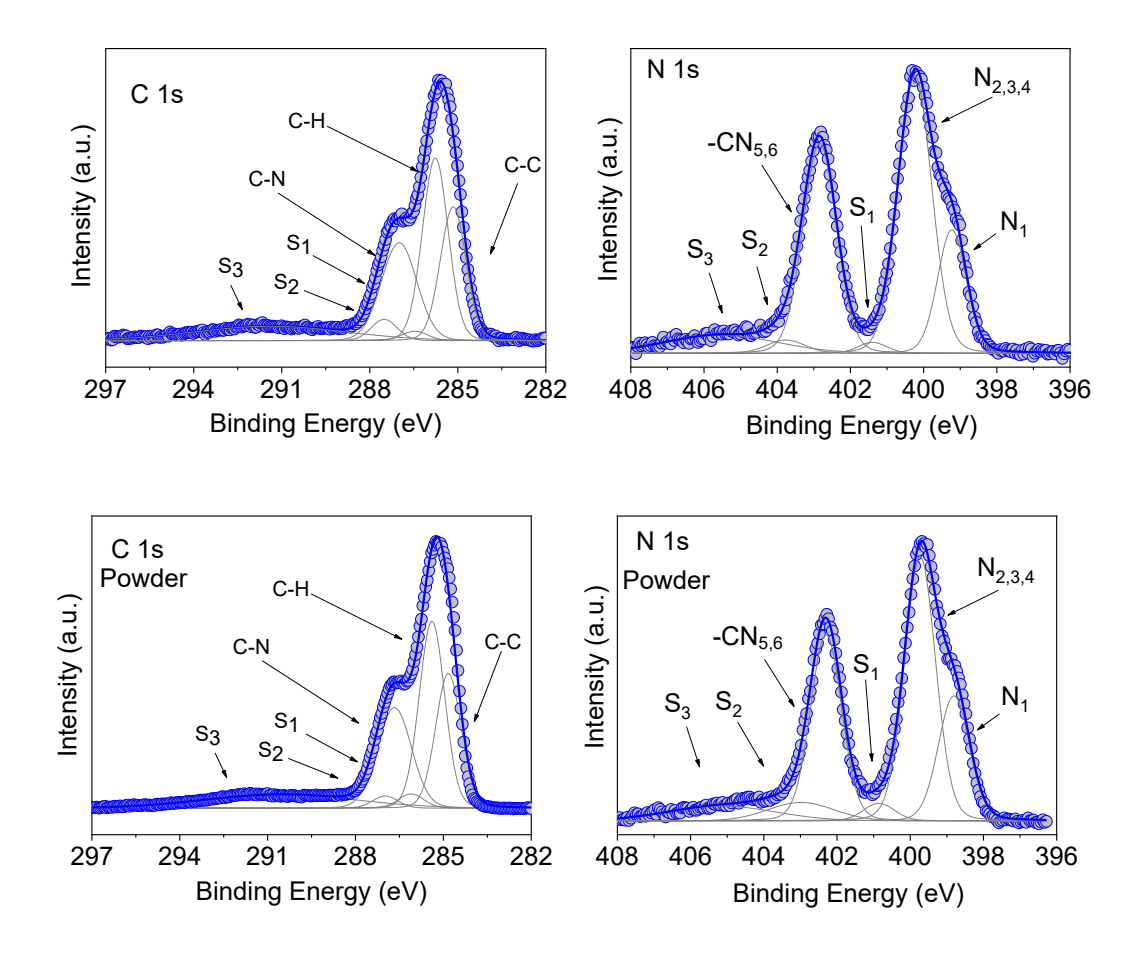


Figure 10. (upper panel) C 1s and N 1s core-level spectra of a thicker assembly of radical **1** deposited on SiO₂/Si(111) substrate compared to the powder spectra (lower panel), together with their fit components,. For the fit details see the Supporting Information.

XPS is also a powerful spectroscopic method to assess the growth modes of adsorbates onto a substrate. An advantage of this method is that the investigation occurs in real time, without breaking the vacuum, by monitoring the decay of the substate signal versus the nominal thickness of the adsorbate during evaporation (Figure 11). We note that the substrate signal, Si 2p in this case, follows an exponential decay with increasing the assembly nominal thickness, which indicates either Straski-Krastanov (layer(s) + islands) or Volmer-Weber growth modes (islands). However, the decay at higher thickness is different in the two cases: for pure island nucleation and growth, the substrate signal intensity is still very high as in the present case. Thus, XPS hints at the Volmer-Weber growth mode. This growth mode is favored by weak molecule-substrate interactions and the selected thermodynamical conditions determined by substrate and evaporation temperatures. To shed light on the assembly morphology we used scanning electron microscopy (SEM). The SEM images (Figure 11 and Fig. S32, SI) are very surprising. On the one hand, they confirm the XPS finding of island growth, on the other hand, the islands have a specific morphology: they are needles. We have never observed this morphology in our previously investigated radical and multiradical systems. This specific morphology justifies, and it is the reason why, in this case, we prefer to use the word "assembly" rather than the word "film" to describe the adsorbate. In general, the needle morphology is generated by the asymmetry of the diffusion and traverse step-edge potential barriers seen by the molecules landing on the nucleated island during evaporation. 92 The diffusion barrier along the plane perpendicular to the needle axis is high, hindering the growth in those directions while the growth along the needle axis is facilitated. We also observe that in some cases the diffusion barrier relaxes giving rise to branches that follow a dendritic growth. The nanoneedles are stable when exposed to air: we monitored their core-level signals upon prolonged air exposure by using XPS and did not observe changes (see: Figs. S33 and S34, SI).

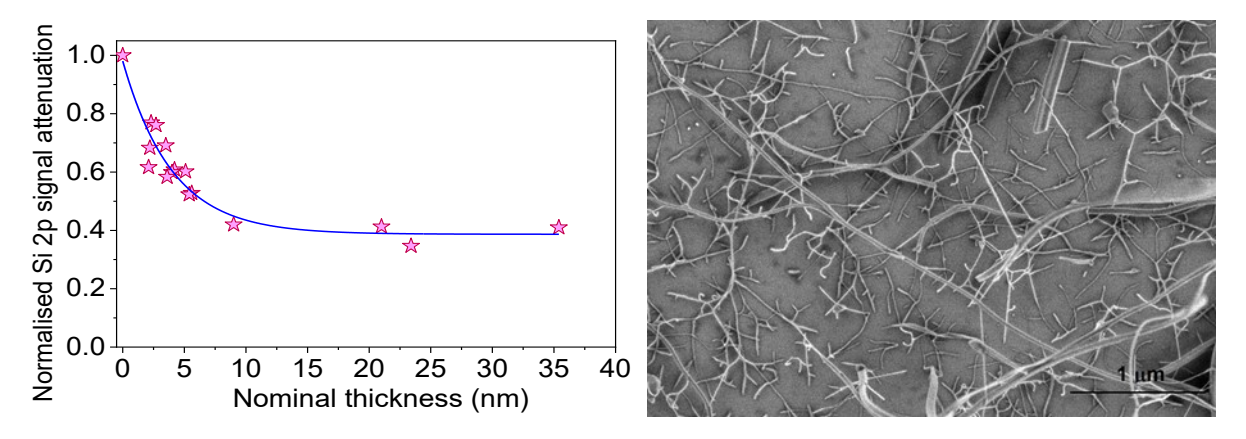


Figure 11. (left) Attenuation of the Si 2p XPS signal, normalized to the corresponding substrate signal at zero adsorbate thickness as a function of radical 1 nominal thickness, during the deposition at room temperature of radical 1. The exponential decay line is a guide to the eye. (right) A typical SEM image showing the radical 1 nanoneedles (see also Fig. S32 in supporting information for additional SEM images).

Persistence of assemblies of radical 1 on silicon surface by EPR spectroscopy. We studied the nanoneedle assemblies of 1 on $SiO_2/Si(111)$ by EPR spectroscopy. Their typical EPR spectra show two components, that is, a narrow $S = \frac{1}{2}$ isotropic peak, which is superimposed on a broader anisotropic $S = \frac{1}{2}$ peaks; these peaks correspond to radical 1 and the well-known paramagnetic defect site in the Si substrate, respectively (Figure 12A). This is confirmed by the spectra of empty $SiO_2/Si(111)$ substrate (SI). Numerical fits of the spectra of the assemblies provide the ratios for the two components, which allow for a calculation of the molar fraction of radical 1, x (Table S12, SI), assuming that the intensity of the spectrum for the Si-defect site is constant. Decay of x follows first-order kinetics with a half-life, $\tau_{1/2} = 50 \pm 4$ days (d) (Figure 12A).

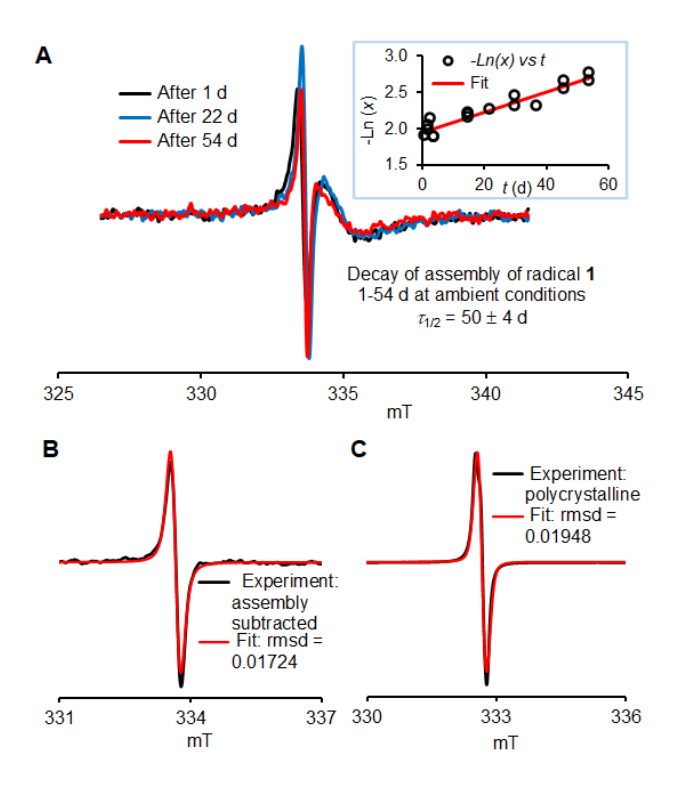


Figure 12. EPR spectroscopy of assemblies of radical **1** at ambient conditions: assemblies on SiO₂/Si(111) (A and B) and polycrystalline (C). Additional details may be found in the SI: Table S12 and Figs. S35–S40.

For the freshly prepared assemblies on SiO₂/Si(111), the spectral subtraction (adsorbate minus the substrate), provides a narrow line spectrum with g = 2.0036 and a peak-to-peak linewidth (lwpp) of about 0.17 mT and 0.12 mT for Gaussian and Lorentzian components (Figure 12B). This spectrum may be compared to similar spectra of polycrystalline radical 1, for which g = 2.0034 and lwpp = 0.18 mT (Gaussian) and 0.05 mT (Lorentzian) are obtained (Figure 12C). Since nanoneedle assemblies have a line-shape intermediate between Gaussian and Lorentzian, this may suggest an even more pronounced 1-D character for exchange coupling, compared to the polycrystalline solid. ⁹³

3. Conclusion

We successfully synthesized two new tetrazolinyl-based (BFTZ) radicals 1 and 2 with excellent spin concentrations. X-ray crystallography of 1 and 2 shows nearly perfectly planar structures. DFT computations reveal perfectly planar structures with C_{2v} (for 1) and C_s (for 2) point groups of symmetry. Di-cyano-substituted radical 1 shows long electron spin coherence times in frozen solution.

Polycrystalline 1 has an ultra-robust thermal stability as suggested by its onset of decomposition in TGA at >260 °C. We were able to evaporate radical 1 under controlled conditions to form nanoneedles with intact radical character. The nanoneedles are also stable under air. This specific morphology might enable using radical 1 with the purpose to achieve precise lateral control of deposition, growth, and positioning of radical nanostructures in nanodevices. Combination of ultra-robust thermal stability, nanoneedle morphology, low electrochemical band gap, and relatively long electron spin coherence times make radical 1 exceptional.

We envisage tetrazolinyl-based (BFTZ) radicals as superior building blocks for next generation of thermally and magnetically robust high-spin diradicals and triradicals.

EXPERIMENTAL SECTION

X-ray crystallography. Crystals of 1 and 2 for X-ray studies were prepared by slow evaporation from organic solvents. Data collections were performed at Indiana University, using Mo Kα radiation. Final cell constants were calculated from the xyz centroids of strong reflections from the actual data collection after integration (SAINT);⁹⁴ intensity data were corrected for absorption (SADABS).⁹⁵ The space group, *P*2₁/n, was determined based on intensity statistics and systematic absences. The structures were solved and refined using the SHELX suite of programs.^{96,97} Intrinsic-methods solutions were calculated, which provided most non-hydrogen atoms from the E-maps. Full-matrix least squares / difference Fourier cycles were performed, which located the remaining non-hydrogen atoms. All non-hydrogen atoms were refined with anisotropic displacement parameters. The hydrogen atoms were placed in ideal positions and refined as riding atoms with relative isotropic displacement parameters. Crystal and structure refinement data for 1 and 2 are in the Supporting Information and the CCDC deposited files in CIF format.

Synthesis. Standard techniques for synthesis under inert atmosphere (argon or nitrogen), using custom-made Schlenk glassware and custom-made double manifold high vacuum lines, were employed. Chromatographic separations were carried out using normal phase neutral alumina or silica gel.

Electron spin relaxation. Pulse EPR data were recorded at X-band on a Bruker E580 spectrometer equipped with an MD4 dielectric resonator and a Bruker/ColdEdge cryogen-free sample cooling system. The sample in 4 mm O.D. was prepared in toluene with a concentration of 200 μ M, validated by spin quantification. The sample was purged with argon for 3 minutes before freezing. Longitudinal relaxation times T_1 were determined from inversion recovery data recorded with a π -T- π /2- τ - π - τ - echo sequence, with a constant τ = 200 ns and four-step phase cycling. Phase memory times $T_{\rm m}$ were obtained from fitting a stretched exponential to Hahn echo decay curves, obtained with a π /2- τ - π - τ - echo sequence, with an initial τ = 200 ns and two-step phase cycling. All pulses are rectangular pulses. The length of the π /2 pulse ranges from 14 ns to 16 ns. A nutation experiment and an echo-detected field sweep were measured at each temperature for optimizing pulse length and magnetic field, respectively. The sample temperature was controlled via a Mercury iTC controller (Oxford Instruments) utilizing a Cernox sensor mounted on the resonator body.

Assemblies on SiO₂/Si(111) wafers. The preparation of the radical assemblies and the XPS measurements were carried out under ultra-high vacuum conditions. A three-chamber UHV-System was used equipped with a monochromatic Al Kα source (SPECS Focus 500) and a SPECS Phoibos 150 MCD hemispherical electron analyzer, attached directly to the OMBD and sample preparation chambers. To grow the radical assemblies on SiO₂/n-Si(111) wafers, we followed our approach to film deposition by OMBD. The substrate was cleaned in an ultrasonic bath in acetone and methanol for one hour each. After annealing at around 500 K for several hours, the wafer surface was examined for contaminants by XPS. The radical molecules were evaporated and deposited on the substrate kept at room temperature (evaporation rate: 0.1–0.7 nm/min). The evaporation rate was monitored by a quartz crystal microbalance. In parallel, the nominal thickness was estimated from the XPS data, investigating the attenuation of the substrate Si 2p signal after deposition. The XPS survey spectra were recorded at 50 eV pass energy and the high-resolution core-level spectra at 20 eV pass energy. All measured binding energies were calibrated by taking the substrate Si 2p_{3/2} signal at 99.8 eV as a reference. The parallel of the parallel of the passence of the substrate Si 2p_{3/2} signal at 99.8 eV as a reference.

photoemission measurements were performed in normal emission. The SEM images were acquired ex-

situ by using a Hitachi SU 8030 SEM.

ASSOCIATED CONTENT

Supporting Information

General procedures and materials, additional experimental and computational details for 1 and 2,

including XPS fit parameters and stability investigations of assemblies of 1. This material is available free

of charge via the Internet at http://pubs.acs.org.

Accession Codes

CCDC 2253237-2253239 contain the supplementary crystallographic data for this paper. These data

can be obtained free of charge via www.ccdc.cam.ac.uk/data request/cif, or by emailing

data request@ccdc.cam.ac.uk, or by contacting The Cambridge Crystallographic Data Centre, 12 Union

Road, 495 Cambridge CB2 1EZ, UK; fax: +44 1223 336033.

AUTHOR INFORMATION

* Corresponding Authors

Andrzej Rajca: e-mail, arajca1@unl.edu

Maria Benedetta Casu: e-mail, benedetta.casu@uni-tuebingen.de

Stefan Stoll: e-mail, stst@uw.edu

Notes

The authors declare no competing financial interests.

22

ACKNOWLEDGMENTS

We thank Haoxin Guo and Dr. Chan Shu, University of Nebraska, for their help with characterization of the radicals and synthetic intermediates. We thank Alexander Batelaan for his synthesis of 4-Br and 5-Br, and acknowledge UCARE program at University of Nebraska for his support. We thank Elke Nadler, Institute of Physical and Theoretical Chemistry, University of Tübingen, for the SEM measurements. We are grateful to the National Science Foundation (NSF), Chemistry Division, for support of this research under Grants CHE-1955349 and CHE-2247170 (A.R.), and CHE-2154302 (S.S.). The upgrade of the EPR spectrometer at Nebraska was funded by the National Institutes of Health (NIH) (NIGMS #R01GM124310-01 to S.R. and A.R.). The upgrade of the EPR spectrometer at Washington was funded by NIH (S10OD021557). Support for the acquisition of the Bruker Venture D8 diffractometer through the Major Scientific Research Equipment Fund from the President of Indiana University and the Office of the Vice President for Research is gratefully acknowledged. The SEM was funded by the DFG under the contract INST 37/829-1 FUGG. Financial support from the German Research Foundation (DFG, contract CA852/11-3) is gratefully acknowledged. This work was partly supported by the European Union's Horizon 2020 Research and Innovation programme under grant agreement no. 965046, FET-Open project Interfast (Gated INTERfaces for FAST information processes).

REFERENCES

- (1) Ciccullo, F.; Gallagher, N. M.; Geladari, O.; Chasse, T.; Rajca, A.; Casu, M. D. A Derivative of the Blatter Radical as a Potential Metal-Free Magnet for Stable Thin Films and Interfaces. *ACS Appl. Mater. Interfaces* **2016**, *8*, 1805–1812.
- (2) Zheng, Y.; Miao, M.-S.; Kemei, M. C.; Seshadri, R.; Wudl, F. The Pyreno-Triazinyl Radical Magnetic and Sensor Properties. *Isr. J. Chem.* **2014**, *54*, 774–778.
- (3) Gallagher, N. M.; Bauer, J. J.; Pink, M.; Rajca, S.; Rajca, A. High-Spin Organic Diradical with Robust Stability. *J. Am. Chem. Soc.* **2016**, *138*, 9377–9380.

- (4) Gallagher, N.; Zhang, H.; Junghoefer, T.; Giangrisostomi, E.; Ovsyannikov, R.; Pink, M.; Rajca, S.; Casu, M. B.; Rajca, A. Thermally and Magnetically Robust Triplet Ground State Diradical. *J. Am. Chem. Soc.* **2019**, *141*, 4764–4774.
- (5) Shu, C.; Pink, M.; Junghoefer, T.; Nadler, E.; Rajca, S.; Casu, M. B.; Rajca, A. Synthesis and Thin Films of Thermally Robust Quartet (*S* = 3/2) Ground State Triradical. *J. Am. Chem. Soc.* **2021**, *143*, 5508–5518.
- (6) Zhang, S.; Pink, M.; Junghoefer, T.; Zhao, W.; Hsu, S.-N.; Rajca, S.; Calzolari, A.; Boudouris, B. W.; Casu, M. B.; Rajca, A. High-Spin (*S* = 1) Blatter-Based Diradical with Robust Stability and Electrical Conductivity. *J. Am. Chem. Soc.* **2022**, *144*, 6059–6070.
- (7) Junghoefer, T.; Calzolari, A.; Baev, I.; Glaser, M.; Ciccullo, F.; Giangrisostomi, E.; Ovsyannikov, R.; Kielgast, F.; Nissen, M.; Schwarz, J.; Gallagher, N. M.; Rajca, A.; Martins, M.; Casu, M. B. Magnetic behavior in metal-free radical thin films. *Chem.* **2022**, *8*, P801–814.
- (8) Rogers, F. J. M.; Norcott, P. L.; Coote, M. L. Recent advances in the chemistry of benzo[e][1,2,4]triazinyl radicals. *Org. Biomol. Chem.* **2020**, *18*, 8255–8277. DOI: 10.1039/D0OB01394C
- (9) Jasiński, M.; Szczytko, J.; Pociecha, D.; Monobe, H.; Kaszyński, P. Substituent-dependent magnetic behavior of discotic benzo[*e*][1,2,4]triazinyls. *J. Am. Chem. Soc.* **2016**, *138*, 9421– 9424, DOI: https://doi.org/10.1021/jacs.6b06444
- (10) Cigl, M.; Pociecha, D.; Jakubowski, R.; Kapuściński, S.; Kaszyński, P. Paramagnetic Liquid Crystals with Close π–π Packing: The Effect of Blatter Radical Planarization on Behavior of Bent-Core Mesogens. *Chem. Eur. J.* 2023, 29, e202203288. DOI: https://doi.org/10.1002/chem.202203288
- (11) Steen, J. S.; Nuismer, J. L.; Eiva, V.; Wiglema, A. E. T.; Daub, N.; Hjelm, J.; Otten, E. Blatter Radicals as Bipolar Materials for Symmetrical Redox-Flow Batteries. *J. Am. Chem. Soc.* **2022**, *144*, 5051–5058. DOI: https://doi.org/10.1021/jacs.1c13543
- (12) Poryvaev, A. S.; Gjuzi, E.; Polyukhov, D. M.; Hoffmann, F.; Frçba, M.; Fedin, M. V. Blatter-Radical-Grafted Mesoporous Silica as Prospective Nanoplatform for Spin Manipulation at Ambient Conditions. *Angew. Chem. Int. Ed.* **2021**, *60*, 8683–8688.
- (13) Neugebauer, F. A. Hydrazidinyl Radicals: 1,2,4,5-Tetraazapentenyls, Verdazyls, and Tetrazolinyls. *Angew. Chem. Int. Ed. Engl.* **1973**, *12*, 455–464.
- (14) Ovchinnikov, A. A. Multiplicity of the ground state of large alternant organic molecules with conjugated bonds. *Theor. Chim. Acta* **1978**, *47*, 297–304.
- (15) Rajca, A. Organic diradicals and polyradicals: from spin coupling to magnetism?. *Chem. Rev.* **1994**, *94*, 871–893.

- (16) Gallagher, N. M.; Olankitwanit, A.; Rajca, A. High-Spin Organic Molecules. *J. Org. Chem.* **2015**, 80, 1291–1298.
- (17) Zhang, H.; Pink, M.; Wang, Y.; Rajca, S.; Rajca, A. High-Spin S = 3/2 Ground-State Aminyl Triradicals: Toward High-Spin Oligo-Aza Nanographenes. *J. Am. Chem. Soc.* **2022**, *144*, 19576–19591.
- (18) McConnell, H. M.; Chesnut, D. B. Theory of Isotropic Hyperfine Interactions in π -Electron Radicals. *J. Chem. Phys.* **1958**, *28*, 107–117.
- (19) Neugebauer, F. A. Elektronenspinsesonanz substituierter Kuhn-Jerchel-Radikale. *Chem. Ber.* **1969**, *102*, 1339–1346.
- (20) Neugebauer, F. A.; Umminger, I. Uber 1,4-Dihydro-l,2,4-benzotriazinyl-Radikale. *Chem. Ber.* **1980**, *113*, 1205–1225.
- (21) Neugebauer, F. A.; Rimmler, G. Endor and Triple Resonance Studies of 1,4-Dihydro-1,2,4-Benzotriazinyl Radicals and 1,4-Dihydro-1,2,4-Benzotriazine Radical Cations. *Magn. Reson. Chem.* **1988**, 26, 595–600.
- (22) Neugebauer, F. A.; Fischer, H.; Krieger, C. Verdazyls. Part 33. EPR and ENDOR studies of 6-oxo- and 6-thioxoverdazyls. X-Ray molecular structure of 1,3,5-triphenyl-6-oxoverdazyl and 3-*tert*-butyl-1,5-diphenyl-6-thioxoverdazyl. *J. Chem. Soc., Perkin Trans* 2, **1993**, 535–544.
- (23) Neugebauer, F. A.; Brunner, H.; Hausser, K. H. Spin densities in 1,3,5-triphenylverdazyl: an NMR study. *Tetrahedron* **1971**, *27*, 3623–3628.
- (24) Neugebauer, F. A. Substituted 5-*t*-butyl tetrazolinyl and phototetrazolinyl radicals. *Tetrahedron* **1970**, *26*, 4843-4851.
- (25) Jerchel, D.; Fischer, H. 2,3-Diphenylen-tetrazoliumsalze und daraus entstehende Radicale. *Liebigs Annalen der Chemie* **1954**, *590*, 216–231.
- (26) Kuhn R.; Jerchel, D. Kristallisiertes 2,3-Diphenylen-5-phenyl-tetrazolium-Radikal. *Liebigs Annalen der Chemie* **1952**, *578*, 1–5.
- (27) Kanal, F.; Schleier, D.; Nuernberger, P. Ultrafast Photogeneration of a Tetrazolinyl Radical. *ChemPhysChem* **2015**, *16*, 3143–3146
- (28) Bolze, T.; Were, J.-L.; Kanal, F.; Schleier, D.; Nuernberger, P. Ultrafast Dynamics of a Fluorescent Tetrazolium Compound in Solution. *ChemPhysChem* **2018**, *19*, 138–147.
- (29) Cademartiri, L.; Ozin, G. A. Ultrathin Nanowires—A Materials Chemistry Perspective. *Adv. Mater.* **2009**, *21*, 1013–1020.

- (30) Yavuz, C. T.; Mayo, J. T.; Yu, W. W.; Prakash, A.; Falkner, J. C.; Yean, S.; Cong, L.; Shipley, H. J.; Kan, A.; Tomson, M.; Natelson, D.; Colvin, V. L. Low-Field Magnetic Separation of Monodisperse Fe₃O₄ Nanocrystals. *Science* 2006, 314, 964–967.
- (31) Yuan, J.; Liu, X.; Akbulut, O.; Hu, J.; Suib, S. L.; Kong, J.; Stellacci, F. Superwetting nanowire membranes for selective absorption. *Nat. Nanotechnol.* **2008**, *3*, 332–336.
- (32) Hasegawa, M.; Iyoda, M. Conducting supramolecular nanofibers and nanorods. *Chem. Soc. Rev.* **2010**, *39*, 2420–2427.
- (33) Briseno, A. L.; Mannsfeld, S. C. B.; Jenekhe, S. A.; Bao, Z.; Xia, Y. Introducing organic nanowire transistors. *Mater. Today* **2008**, *11*, 38–47.
- (34) Savu, S.-A.; Sonström, A.; Bula, R.; Bettinger, H. F.; Chassé, T.; Casu, M. B. Intercorrelation of Electronic, Structural, and Morphological Properties in Nanorods of 2,3,9,10-Tetrafluoropentacene. *ACS Appl. Mater. Interfaces* **2015**, *7*, 19774–19780.
- (35) Savu, S. A.; Abb, S.; Schundelmeier, S.; Saathoff, J. D.; Stevenson, J. M.; Toenshoff, C.; Bettinger, H. F.; Clancy, P.; Casu, M. B.; Chassé, T. Pentacene-based nanorods on Au(111) single crystals: Charge transfer, diffusion, and step-edge barriers. *Nano Research* **2013**, *6*, 449–459.
- (36) Kowarik, S.; Gerlach, A.; Hinderhofer, A.; Milita, S.; Borgatti, F.; Zontone, F.; Suzuki, T.; Biscarini, F.; Schreiber, F. Structure, morphology, and growth dynamics of perfluoro-pentacene thin films. *Phys. Status Solidi RRL* **2008**, *2*, 120–122.
- (37) Günder, D.; Diez-Cabanes, V.; Huttner, A.; Breuer, T.; Lemaur, V.; Cornil, J.; Witte, G. F-Center-Mediated Growth of Patterned Organic Semiconductor Films on Alkali Halides. *ACS Appl. Mater. Interfaces* **2022**, *14*, 46086–46094.
- (38) Gutiérrez, D.; Riera-Galindo, S.; Ajayakumar, M. R.; Veciana, J.; Rovira, C.; Mas-Torrent, M.; Crivillers, N. Self-Assembly of an Organic Radical Thin Film and Its Memory Function Investigated Using a Liquid-Metal Electrode. *J. Phys. Chem. C.* **2018**, *122*, 17784–17791.
- (39) Katritzky, A. A.; Belyakov, S. A.; Cheng, D.; Durst, H. D. Syntheses of Formazans Under Phase-Transfer Conditions. *Synthesis* **1995**, *1995*, 577–581.
- (40) Hegarty, A. F.; Scott, F. L. Kinetics and Mechanism of the Formation of Formazans by Diazonium Ion Attack on Hydrazones. *J. Org. Chem.* **1967**, *32*, 1957–1963.
- (41) Nineham, A. W. The chemistry of formazans and tetrazolium salts. *Chem. Rev.* **1955**, *55*, 355–483.
- (42) Bondi, A. Van der Waals Volumes and Radii. J. Phys. Chem. **1964**, 68, 441–451.

- (43) Frisch, M. J.; Trucks, G. W.; Schlegel, H. B.; Scuseria, G. E.; Robb, M. A.; Cheeseman, J. R.; Scalmani, G.; Barone, V.; Petersson, G. A.; Nakatsuji, H.; Li, X.; Caricato, M.; Marenich, A. V.; Bloino, J.; Janesko, B. G.; Gomperts, R.; Mennucci, B.; Hratchian, H. P.; Ortiz, J. V.; Izmaylov, A. F.; Sonnenberg, J. L.; Williams-Young, D.; Ding, F.; Lipparini, F.; Egidi, F.; Goings, J.; Peng, B.; Petrone, A.; Henderson, T.; Ranasinghe, D.; Zakrzewski, V. G.; Gao, J.; Rega, N.; Zheng, G.; Liang, W.; Hada, M.; Ehara, M.; Toyota, K.; Fukuda, R.; Hasegawa, J.; Ishida, M.; Nakajima, T.; Honda, Y.; Kitao, O.; Nakai, H.; Vreven, T.; Throssell, K.; Montgomery, J. A., Jr.; Peralta, J. E.; Ogliaro, F.; Bearpark, M. J.; Heyd, J. J.; Brothers, E. N.; Kudin, K. N.; Staroverov, V. N.; Keith, T. A.; Kobayashi, R.; Normand, J.; Raghavachari, R.; Rendell, A. P.; Burant, J. C.; Iyengar, S. S.; Tomasi, J.; Cossi, M.; Millam, J. M.; Klene, M.; Adamo, C.; Cammi, R.; Ochterski, J. W.; Martin, R. L.; Morokuma, K.; Farkas, O.; Foresman, J. B.; Fox, D. J. *Gaussian 16*, revision A.03; Gaussian, Inc.: Wallingford, CT, 2016.
- (44) Grimme, S.; Antony, J.; Ehrlich, S.; Krieg, H. A consistent and accurate ab initio parametrization of density functional dispersion correction (DFT-D) for the 94 elements H-Pu. *J. Chem. Phys.* **2010**, *132*, 154104–154118.
- (45) Grimme, S.; Ehrlich, S.; Goerigk, L. Effect of the damping function in dispersion corrected density functional theory. *J. Comput. Chem.* **2011**, *32*, 1456–1465.
- (46) Gryn'ova, G.; Marshall, D. L.; Blanksby, S. J.; Coote, M. L. Switching radical stability by pH-induced orbital conversion. *Nat. Chem.* **2013**, *5*, 474–481.
- (47) Wang, Y.; Zhang, H.; Pink, M.; Olankitwanit, A.; Rajca, S.; Rajca, A. Radical Cation and Neutral Radical of Aza-thia[7]helicene with SOMO–HOMO Energy Level Inversion. *J. Am. Chem. Soc.* **2016**, *138*, 7298–7304.
- (48) Shu, C.; Zhang, H.; Olankitwanit, A.; Rajca, S.; Rajca, A. High-Spin Diradical Dication of Chiral π-Conjugated Double Helical Molecule. *J. Am. Chem. Soc.* **2019**, *141*, 17287–17294.
- (49) Kasemthaveechok, S.; Abella, L.; Jean, M.; Cordier, M.; Roisnel, T.; Vanthuyne, N.; Guizouarn, T.; Cador, O.; Autschbach, J.; Crassous, J.; Favereau, L. Axially and Helically Chiral Cationic Radical Bicarbazoles: SOMO-HOMO Level Inversion and Chirality Impact on the Stability of Mono- and Diradical Cations. J. Am. Chem. Soc. 2020, 142, 20409–20418.
- (50) Abella, L.; Crassous, J.; Favereau, L.; Autschbach, J. Why is the Energy of the Singly Occupied Orbital in Some Radicals below the Highest Occupied Orbital Energy? *Chem. Mater.* **2021**, *33*, 3678–3691.
- (51) Kasemthaveechok, S.; Abella, L.; Jean, M.; Cordier, M.; Vanthuyne, N.; Guizouarn, T.; Cador, O.; Autschbach, J.; Crassous, J.; Favereau, L. Carbazole Isomerism in Helical Radical Cations: Spin

- Delocalization and SOMO-HOMO Level Inversion in the Diradical State. *J. Am. Chem. Soc.* **2022**, *144*, 7253–7263.
- (52) Kasemthaveechok, S.; Abella, L.; Crassous, J.; Autschbach, J.; Favereau, L. Organic radicals with inversion of SOMO and HOMO energies and potential applications in optoelectronics. *Chem. Sci.* **2022**, *13*, 9833–9847. DOI: https://doi.org/10.1039/D2SC02480B
- (53) Neugebauer, F. A.; Russell, G. A. Tetrazolinyl Radicals. J. Org. Chem. 1968, 33, 2744–2746.
- (54) Stoll, S.; Schweiger, A. EasySpin, a comprehensive software package for spectral simulation and analysis in EPR. *J. Magn. Reson.* **2006**, *178*, 42–55.
- (55) Dzuba, S. A.; Maryasov, A. G.; Salikhov, K. M.; Tsvetkov, Yu. D. Superslow rotations of nitroxide radicals studied by pulse EPR spectroscopy. *J. Magn. Reson.* 1984, 58, 95–117. DOI: 10.1016/0022-2364(84)90010-6
- (56) Zecevic, A.; Eaton, G. R.; Eaton, S. S.; Lindgren, M. Dephasing of electron spin echoes for nitroxyl radicals in glassy solvents by non-methyl and methyl protons. *Mol. Phys.* **1998**, *95*, 1255–1263, DOI: 10.1080/00268979809483256
- (57) Kveder, M.; Rakvin, B.; You, J. A quantum many body model for the embedded electron spin decoherence in organic solids. *J. Chem. Phys.* **2019**, *151*, 164124. DOI: https://doi.org/10.1063/1.5124561
- (58) Huang, S.; Pink, M.; Ngendahimana, T.; Rajca, S.; Eaton, G. R.; Eaton, S. S.; Rajca, A. Bis-Spiro-Oxetane and Bis-Spiro-Tetrahydrofuran Pyrroline Nitroxide Radicals: Synthesis and Electron Spin Relaxation Studies. *J. Org. Chem.* **2021**, *86*, 13636–13643. DOI: https://doi.org/10.1021/acs.joc.1c01670
- (59) Zadrozny, J. M.; Niklas, J.; Poluektov, O. G.; Freedman, D. E. Millisecond Coherence Time in a Tunable Molecular Electronic Spin Qubit. *ACS Cent. Sci.* **2015**, *1*, 488–492. DOI: https://doi.org/10.1021/acscentsci.5b00338.
- (60) Yu, C.-J.; von Kugelgen, S.; Laorenza, D. W.; Freedman, D. E. A Molecular Approach to Quantum Sensing. *ACS Cent. Sci.* **2021**, 7, 712–723. DOI: https://doi.org/10.1021/acscentsci.0c00737.
- (61) Ciccullo, F.; Calzolari, A.; Bader, K.; Neugebauer, P.; Gallagher, N. M.; Rajca, A.; van Slageren, J.; Casu, M. B., Interfacing a Potential Purely Organic Molecular Quantum Bit with a Real-Life Surface. ACS Appl. Mater. Interfaces 2019, 11, 1571–1578.
- (62) Kahn, O. Molecular magnetism, Wiley-VCH, New York, 1993, Ch. 11, p. 272.
- (63) Xiang, T. Thermodynamics of quantum Heisenberg spin chains. *Phys. Rev. B* **1998**, *58*, 9142–9149. DOI: https://doi.org/10.1103/PhysRevB.58.9142

- (64) Breunig, O.; Garst, M.; Klümper, A.; Rohrkamp, J.; Turnbull, M. M.; Lorenz, T. Quantum criticality in the spin-1/2 Heisenberg chain system copper pyrazine dinitrate. *Sci. Adv.* **2017**, *3*, eaao3773. DOI: https://doi.org/10.1126/sciadv.aao3773
- (65) Rajca, A.; Takahashi, M.; Pink, M.; Spagnol, G.; Rajca, S. Conformationally constrained, stable, triplet ground state (*S* = 1) nitroxide diradicals: antiferromagnetic chains of *S* = 1 diradicals. *J. Am. Chem. Soc.* **2007**, *129*, 10159–10170. DOI: https://doi.org/10.1021/ja0712017
- (66) Wang, W.; Chen, C.; Shu, C.; Rajca, S.; Wang, X.; Rajca, A. *S* = 1 Tetraazacyclophane Diradical Dication with Robust Stability: a Case of Low Temperature One-Dimensional Antiferromagnetic Chain. *J. Am. Chem. Soc.* **2018**, *140*, 7820–7826.
- (67) Connelly, N. G.; Geiger, W. E. Chemical Redox Agents for Organometallic Chemistry. *Chem. Rev.* **1996**, *96*, 877–910.
- (68) Hutchison, K. A.; Srdanov, G.; Menon, R.; Gabriel, J.-C. P.; Knight, B.; Wudl, F. A Pressure Sensitive Two-Dimensional Tetracyanoquinodimethane (TCNQ) Salt of a Stable Free Radical. *J. Am. Chem. Soc.* **1996**, *118*, 13081–13082.
- (69) Bartos, P.; Anand, B.; Pietrzak, A.; Kaszyński, P. Functional Planar Blatter Radical through Pschorr-Type Cyclization. *Org. Lett.* **2020**, *22*, 180–184.
- (70) Gilroy, J. B.; McKinnon, S. D. J.; Koivisto, B. D.; Hicks, R. G. Electrochemical Studies of Verdazyl Radicals. *Org. Lett.* **2007**, *9*, 4837–4840.
- (71) Tretyakov, E. V.; Petunin, P. V.; Zhivetyeva, S. I.; Gorbunov, D. E.; Gritsan, N. P.; Fedin, M. V.; Stass, D. V.; Samoilova, R. I.; Bagryanskaya, I. Y.; Shundrina, I. K.; Bogomyakov, A. S.; Kazantsev, M. S.; Postnikov, P. S.; Trusova, M. E.; Ovcharenko, V. I. Platform for High-Spin Molecules: A Verdazyl-Nitronyl Nitroxide Triradical with Quartet Ground State. *J. Am. Chem. Soc.* 2021, 143, 8164–8176.
- (72) Pal, S. K.; Itkis, M. E.; Tham, F. S.; Reed, R. W.; Oakley, R. T.; Haddon, R. C. Resonating valence-bond ground state in a phenalenyl-based neutral radical conductor. *Science* **2005**, *309*, 281–284.
- (73) Mailman, A.; Wong, J. W. L.; Winter, S. M.; Claridge, R. C. M.; Robertson, C. M.; Assoud, A.; Yong, W.; Steven, E.; Dube, P. A.; Tse, J. S.; Desgreniers, S.; Secco, R. A.; Oakley, R. T. Fine tuning the performance of multiorbital radical conductors by substituent effects. *J. Am. Chem. Soc.* **2017**, *139*, 1625–1635.
- (74) Joo, Y.; Agarkar, V.; Sung, S. H.; Savoie, B. M.; Boudouris, B. W. A nonconjugated radical polymer glass with high electrical conductivity. *Science* **2018**, *359*, 1391–1395.

- (75) Tan, Y.; Casetti, N. C.; Boudouris, B. W.; Savoie, B. M. Molecular Design Features for Charge Transport in Nonconjugated Radical Polymers. *J. Am. Chem. Soc.* **2021**, *143*, 31, 11994–12002. DOI: https://doi.org/10.1021/jacs.1c02571
- (76) Junghoefer, T.; Gallagher, N. M.; Kolanji, K.; Giangrisostomi, E.; Ovsyannikov, R.; Chassé, T.; Baumgarten, M.; Rajca, A.; Calzolari, A.; Casu, M. B. Challenges in controlled thermal deposition of organic diradicals. *Chem. Mat.* **2021**, *33*, 2019–2028.
- (77) Savu, S.-A.; Casu, M. B.; Schundelmeier, S.; Abb, S.; Tonshoff, C.; Bettinger, H. F.; Chassé, T. Nanoscale assembly, morphology and screening effects in nanorods of newly synthesized substituted pentacenes. *RSC Adv.* **2012**, *2*, 5112–5118.
- (78) Casu, M. B. Nanoscale Studies of Organic Radicals: Surface, Interface, and Spinterface. *Acc. Chem. Res.* **2018**, *51*, 753–760.
- (79) Siegbahn, K.; Nordling, C.; Fahlman, A.; Nordberg, R.; Hamrin, K.; Hedman, J.; Johansson, G.; Bergmark, T.; Karlsson, S.-E.; Lindgren, I.; Lindberg, B. *ESCA*, *Atomic*, *Molecular and Solid State Structure Studied by Means of Electron Spectroscopy*. Almqvist and Wiksells: Uppsala, 1967.
- (80) Siegbahn, K. M. Nobel Lecture: Electron Spectroscopy for Atoms, Molecules and Condensed Matter. http://www.nobelprize.org/nobel_prizes/physics/laureates/1981/siegbahn-lecture.html (accessed 20 March 2023).
- (81) Junghoefer, T.; Nowik-Boltyk, E. M.; de Sousa, J. A.; Giangrisostomi, E.; Ovsyannikov, R.; Chassé, T.; Veciana, J.; Mas-Torrent, M.; Rovira, C.; Crivillers, N.; Casu, M. B. Stability of radical-functionalized gold surfaces by self-assembly and on-surface chemistry. *Chem. Sci.* **2020**, *11*, 9162–9172.
- (82) Dobler, C.; Tönshoff, C.; Bettinger, H. F.; Chassé, T.; Casu, M. B. Cyano-Functional Group as an Anchoring Tool for Organic Small Molecules on Gold. *J. Phys. Chem. C* **2017**, *121*, 13660–13665.
- (83) Travnikova, O.; Børve, K. J.; Patanen, M.; Söderström, J.; Miron, C.; Sæthre, L. J.; Mårtensson, N.; Svensson, S. The ESCA molecule—Historical remarks and new results. *J. Electron. Spectros. Relat. Phenomena* **2012**, *185*, 191–197.
- (84) Du, X.; Wang, S.-Y.; Wei, M.; Zhang, J.-R.; Ge, G.; Hua, W. A theoretical library of N1s core binding energies of polynitrogen molecules and ions in the gas phase. *Phys. Chem. Chem. Phys.* **2022**, *24*, 8196–8207.

- (85) Dietrich, M.; Delaittre, G.; Blinco, J. P.; Inglis, A. J.; Bruns, M.; Barner-Kowollik, C. Photoclickable Surfaces for Profluorescent Covalent Polymer Coatings. *Adv. Funct. Mater.* **2012**, 22, 304–312.
- (86) Wu, Z.; Luo, J.; Liang, Y.; Yu, X.; Zhao, Y.; Li, Y.; Wang, W.; Sui, Z.; Tian, X.; Chen, Q. Tetrazole functionalized benzoquinoline-linked covalent organic frameworks with efficient performance for electrocatalytic H₂O₂ production and Li-S batteries. *Mat. Chem. Front.* **2023**, **7**, 1650–1658.
- (87) Knecht, P.; Suryadevara, N.; Zhang, B.; Reichert, J.; Ruben, M.; Barth, J. V.; Klyatskaya, S.; Papageorgiou, A. C. The self-assembly and metal adatom coordination of a linear bis-tetrazole ligand on Ag(111). *Chem. Commun.* **2018**, *54*, 10072–10075.
- (88) Szőcs, E.; Bakó, I.; Kosztolányi, T.; Bertóti, I.; Kálmán, E. EC-STM study of 5-mercapto-1-phenyl-tetrazole adsorption on Cu(1 1 1). *Electrochim. Acta* **2004**, *49*, 1371–1378.
- (89) Henze, S. K. M.; Bauer, O.; Lee, T. L.; Sokolowski, M.; Tautz, F. S., Vertical bonding distances of PTCDA on Au(111) and Ag(111): Relation to the bonding type. *Surf. Sci.* **2007**, *601*, 1566–1573.
- (90) Zou, Y.; Kilian, L.; Schöll, A.; Schmidt, T.; Fink, R.; Umbach, E., Chemical bonding of PTCDA on Ag surfaces and the formation of interface states. *Surf. Sci.* **2006**, *600*, 1240–1251.
- (91) Kröger, I.; Stadtmüller, B.; Kleimann, C.; Rajput, P.; Kumpf, C. Normal-incidence x-ray standing-wave study of copper phthalocyanine submonolayers on Cu(111) and Au(111). *Phys. Rev. B* **2011**, 83, 195414.
- (92) Savu, S. A.; Abb, S.; Schundelmeier, S.; Saathoff, J. D.; Stevenson, J. M.; Toenshoff, C.; Bettinger, H. F.; Clancy, P.; Casu, M. B.; Chassé, T. Pentacene-based nanorods on Au(111) single crystals: Charge transfer, diffusion, and step-edge barriers. *Nano Research* **2013**, *6*, 449–459.
- (93) Hennessy, M. J.; McElwee, C. D.; Richards, P. M. Effect of interchain coupling on electron-spin resonance in nearly one-dimensional systems. *Phys. Rev. B* **1973**, *7*, 930–947.
- (94) SAINT V8.40A (2020), Bruker AXS, Madison, WI, 2018.
- (95) Krause, L.; Herbst-Irmer, R.; Sheldrick, G. M.; Stalke, D. Comparison of silver and molybdenum microfocus X-ray sources for single-crystal structure determination. *J. Appl. Cryst.* **2015**, *48*, 3–10. doi:10.1107/S1600576714022985.

- (96) Sheldrick, G. M. SHELXT--Integrated space-group and crystal-structure determination. *Acta Cryst. A* **2015**, *71*, 3–8. doi:10.1107/S2053273314026370.
- (97) Sheldrick, G. M. Crystal structure refinement with SHELXL. *Acta Cryst. C* **2015**, *71*, 3–8. doi:10.1107/S2053229614024218.
- (98) Savu, S.-A.; Biswas, I.; Sorace, L.; Mannini, M.; Rovai, D.; Caneschi, A.; Chassé, T.; Casu, M. B. Nanoscale Assembly of Paramagnetic Organic Radicals on Au(111) Single Crystals. *Chem.-Eur. J.* 2013, 19, 3445–3450.
- (99) Moulder, J. F.; Stickle, W. F.; Sobol, P. E.; Bomben, K. D. *Handbook of X-ray Photoelectron Spectroscopy*, (Ed. Chastain, J.), Perkin-Elmer Corp., Physical Electronics Division, Minnesota, United States of America, 1992.

Table of Contents Graphics

